Influence of Scan Strategy on Porosity and Microstructure of Ti-6Al-4V Fabricated by Electron Beam Powder Bed Fusion

Peeyush Nandwana[1]* and Yousub Lee[2]

[1]Materials Science and Technology Division, Oak Ridge National Laboratory, Oak Ridge, USA

[2]Computational Science and Engineering Division, Oak Ridge National Laboratory, Oak Ridge, USA

*Corresponding author: Peeyush Nandwana, nandwanap@ornl.gov, 865-241-1435

Abstract

Ti-6Al-4V is of high value in biomedical, aerospace, and industrial sectors and is ideal for additive manufacturing (AM) owing to its poor machinability. In electron beam powder bed fusion of Ti-6Al-4V raster scan is commonly used and often results in porosity that is detrimental to the fatigue strength. In this paper, we demonstrate that spot melting can significantly minimize porosity but results in a coarser microstructure compared to raster melting. Process parameters can be optimized to achieve minimal porosity with tailored microstructures. Finite element method was used to rationalize these observations.

Keywords: Additive manufacturing, Ti-6Al-4V, Spot melting, Porosity, Electron beam melting

Introduction

In the past decade additive manufacturing (AM) has emerged as a viable technique to fabricate near net shape components, especially for difficult to machine alloys like Ti-6Al-4V. Laser powder bed fusion (LPBF) and electron beam powder bed fusion (EPBF) have been extensively researched for Ti-6Al-4V AM [1–15]. EPBF Ti-6Al-4V consists of columnar β grains along with grain boundary α and intragranular basketweave α [7,12,16]. Defects like lack of fusion porosity (LOF) and gas porosity are common and have a detrimental effect on mechanical properties, especially high cycle fatigue (HCF) [17–20]. Spherical gas pores are believed to originate either from the trapped argon in the powders during atomization or hydrogen pores resulting from breakdown of adsorbed water vapor on the powder surfaces [17]. Hot isostatic processing (HIP) is used for minimization and mitigation of porosity. However, reports concerningly show that gas pores, though closed below detectable limits via HIP, tend to regrow during heat treatment [17,21,22]. Porosity regrowth can limit the heat treatment temperatures or elevated temperature performance of the material. Thus, the focus should be on minimizing porosity during component fabrication via EPBF. There are reports on the role of process parameters on porosity but limited work has been done on exploring new scan strategies to mitigate porosity during EPBF of Ti-6Al-4V [13,18,23]. In this paper, we use a spot melting strategy to mitigate porosity compared to raster melting that is commonly used for EPBF of Ti-6Al-4V. We also discuss the microstructure evolution and use melt pool simulations to rationalize the porosity mitigation and microstructural differences between spot and raster melting. Although, spot melting has been used for modification of microstructure in Inconel 718, there are no reports of using spot melting for EPBF of Ti-6Al-4V to the best of the authors knowledge [24–26].

Methods

An Arcam Q10 EPBF system running software version 4.0.28 was used to fabricate samples using raster and spot melting while maintaining a powder bed temperature of 773 K. In raster scan strategy the speed and power of the beam are varied to maintain a constant melt pool geometry at all points in the build [25]. Spot melting, on the other hand, melts one point at a time thereby making beam current (i_b), beam dwell time (t_d), and point spacing critical process variables [25,27]. The spot melting pattern used in this study is schematically shown in Figure 1(a). After the first spot is melted at the top left corner of the build, the beam skips a predefined number of steps (10 in this case) along the x direction until all the spots are exhausted, following which the beam skips a set number of rows along the y direction (3 in this case) and in that row the first spot to be melted is halfway between the spots melted in the prior row i.e. the very first row, thus completing a triangular pattern. The spot melting order is shown in Figure 1(a). The point spacing i.e. distance between adjacent points was $200\mu m$.

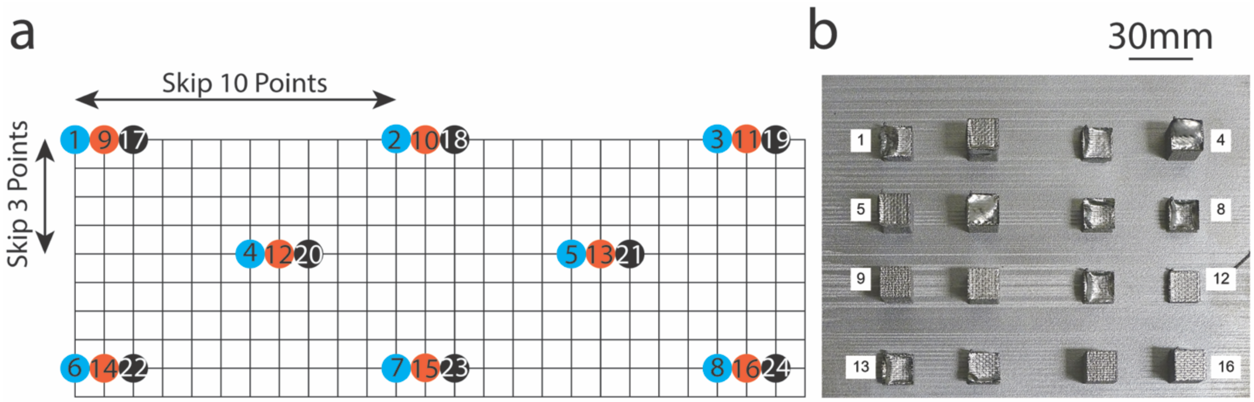

Figure 1 shows (a) the schematic of point melting with the numbers representing the order of melting, and (b) the calibration build that was used for process parameter development

Spot melting was used to fabricate 16 coupons with dimensions $15mm\ (L) \times 15mm(W) \times 25mm(H)$. A total of 8 different process parameter sets were explored and two replicates were deposited at random locations on the start plate using each parameter set to minimize the impact of spatial location. The beam focus offset, an indirect measure of the beam diameter was set at 0 in all cases. Except coupons 9 and 15 (i_b = $12mA$, t_d = $0.1ms$), and 10 and 16 (i_b = $11mA$, t_d = $0.4ms$) all other process conditions result in parts with swelling or delamination. Coupons 9 and 10 were prepared for microstructural examination by conventional metallographic techniques. A Leica DM4000 M LED Optical Microscope was used for imaging the samples that were analyzed using ImageJ for porosity area fraction measurements. The samples were subsequently etched with Kroll's Reagent for microstructure evaluation. A Joel 6500 scanning electron microscope equipped with an EDAX Hikari electron backscatter diffraction (EBSD) system was used for orientation mapping. A 3D multi-physics code Truchas was implemented to quantify the effects of process parameters on porosity and microstructure evolution. A transient volumetric heat source with gaussian distribution was adopted as the heat flux boundary condition for the raster scan while a stationary heat source with pre-defined beam dwell time was developed for spot melting [26]. For the boundary condition, a radiative heat loss was used for the top surface while convective heat loss was neglected owing to the high vacuum conditions during EBPF. Adiabatic conditions were assumed for other surfaces owing to the low thermal conductivity of the powder bed. A preheat temperature of 773K was used as the initial condition. The thermophysical properties and process parameters used in the simulations are summarized in Table 1.

Thermophysical Properties	**Value**	**Unit**
Density of solid	4050	Kg/m^3
Liquidus temperature	1923	K
Solidus temperature	1877	K
Specific heat of liquid	759	J/Kg-K
Specific heat of solid	750	J/Kg-K
Effective thermal conductivity of liquid	426	W/m-K
Thermal conductivity of solid	27	W/m-K
Latent heat	2.86×10^5	J/Kg
Emissivity	0.2	
Viscosity	2.36×10^{-3}	Kg/m-s

Temperature coefficient of surface tension	-0.26×10^{-3}	N/m/K
Process Parameters		
Beam diameter	200	μm
Preheat temperature	773	K
Raster beam speed	4550	mm/s
Raster melting current	28	mA
Point melting beam dwell time	0.1 (coupon 9), 0.4 (coupon 10)	ms
Point melting current	12 (coupon 9), 11 (coupon 10)	mA

Table 1 summarizes the thermophysical properties [28] [29] and process parameters used for simulating the thermal conditions for raster and spot melting

Results

The effects of scan strategy on porosity and microstructure are shown in Figure 2. The samples fabricated using raster melting with Arcam standard parameters had mostly spherical gas porosity with an area fraction of ~1.8% shown in Figure 1(a). Of the two coupons fabricated using spot melting, coupon 9 had significantly higher porosity area fraction (~5.2%) compared to coupon 10 (~0.02%). Coupon 9 has predominantly elongated LOF pores along with spherical gas pores while coupon 10 has only spherical gas pores shown in Figures 2(b) and (c) respectively. The sample processed using raster scan had a basketweave microstructure with an α lath thickness of $1.1\mu m$ shown in Figure 1(d). On the other hand, coupon 9 has a predominantly martensitic microstructure shown in Figure 1(e) with α' laths $<0.5\mu m$ thick while coupon 10 displays a relatively coarser basketweave microstructure with grain boundary α and an average lath thickness of about $1.8\mu m$. In all cases, the prior β grains remain columnar with varying grain diameters indicative of different rates of solidification.

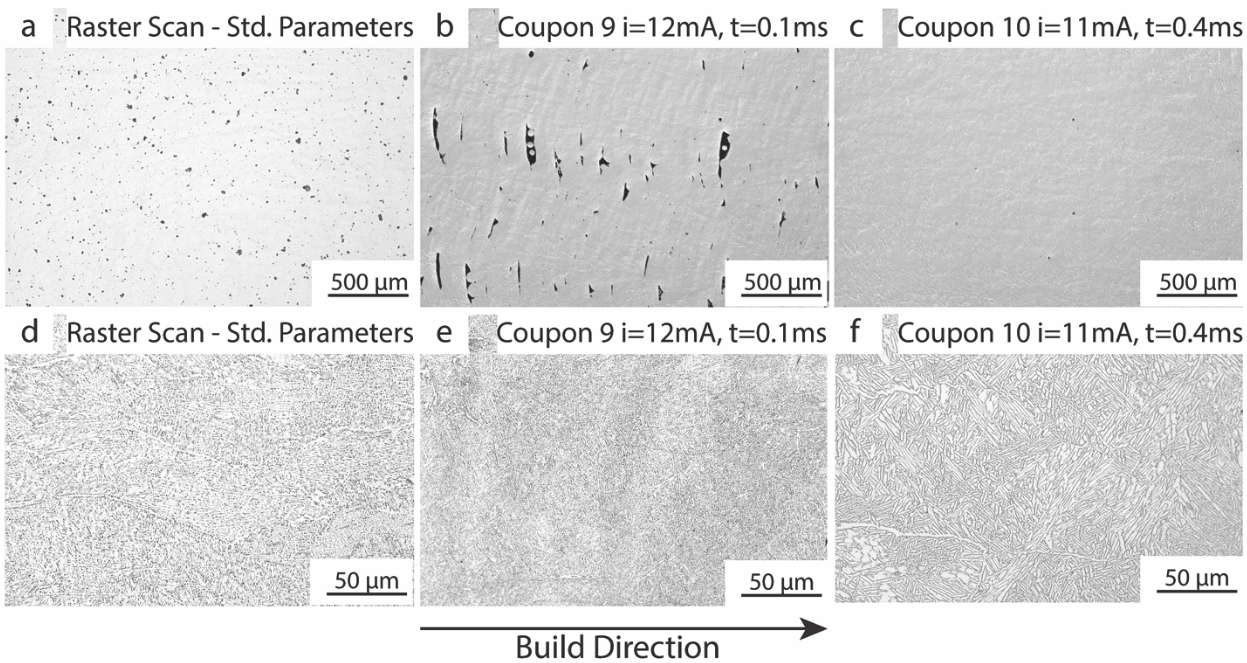

Figure 2 shows the porosity (a-c) and microstructures (d-f) of samples fabricated using raster scan melting and point melting strategies with different process parameters

Figure 3 (a-d) show the melt pool simulations and associated cooling rates for the three processing conditions. To be noted is that coupon 9 has the lowest melt pool depth $(125\mu m)$ and the highest cooling rate below the β-transus $(1.4 \times 10^5\ K/s)$ while coupon 10 has the deepest melt pool $(220\mu m)$ and the slowest cooling rate $(6.9 \times 10^4\ K/s)$ with the raster scan having a melt pool depth $(155\mu m)$ and cooling rate $(1.0 \times 10^5\ K/s)$ intermediate to the two spot melted samples. The smallest melt pool and highest cooling rate explains the LOF porosity and the martensitic microstructure in coupon 9. Although, at cooling rates martensite will be the first phase to evolve per the CCT diagram in Figure 3(d), the smaller melt pool in the case of coupon

9 will result in lesser melt pool overlap as well as less number of remelting cycles experienced by the layers as more layers are deposited on top that can result in the retention of the martensitic structure unlike coupon 10 and the sample processed via raster scan strategy. More complex models are required to accurately describe the effects of thermal cycling on the microstructure evolution and are beyond the scope of the current work. The key differences between the porosity levels and microstructures between raster scan fabricated sample and spot melted coupon need further discussion.

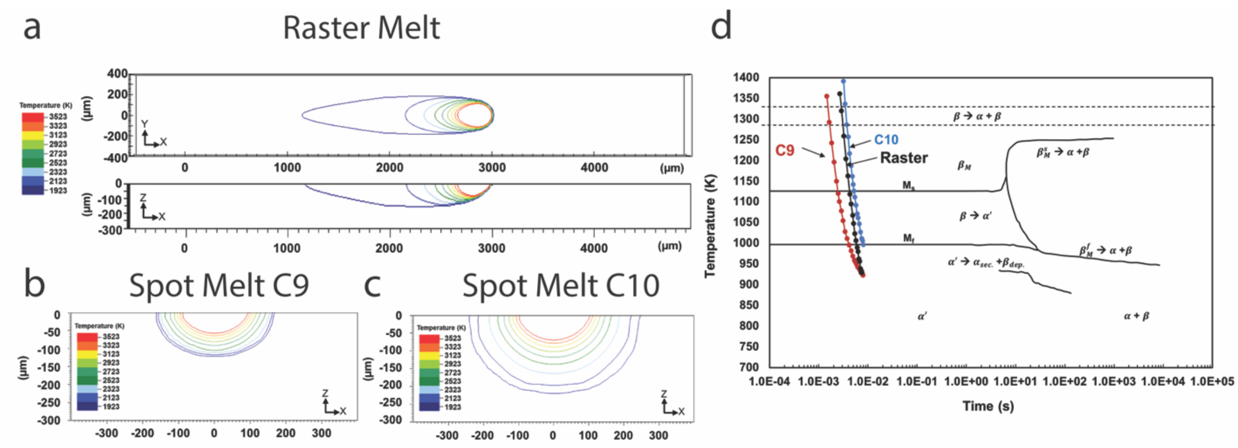

Figure 3 shows the predicted melt pools for (a) raster melt, (b) spot melted coupon 9, (c) spot melted coupon 10, and (d) the cooling curves overlaid on the transformation pathway showing $\beta \rightarrow \alpha'$ transformation

Discussion

First, the mechanism of porosity formation and the impact of spot melting in eliminating the porosity will be discussed. The pores can originate from the hydrogen released by decomposition of adsorbed water vapor on the powders or the trapped argon in powders during atomization. Depending on the beam power and speed, the pores either get trapped in the melt pool during solidification or can escape. The most widely discussed hypothesis for porosity formation in powder bed fusion is based on energy density used for melting. A higher energy density is typically associated with larger melt pool area and subsequently lower porosity [23,30,31]. Figure 4 (a) shows that the measured porosity area fractions vary linearly with volumetric energy density for the three processing conditions used in our study and are in line with observations reported by other researchers. The LOF pores in coupon 9 can be explained based on very low energy density (~11.5 J/mm^3) and the highest energy density for coupon 10 results in the lowest porosity with raster scan in the middle. Although energy density can be effective in explaining average porosity i.e. LOF and gas porosity, it cannot be used to satisfactorily explain the formation of gas porosity alone. The phenomenological explanation is that increasing energy density results in a larger melt pool that takes longer to solidify thereby allowing enough time for the gas pores to escape [18]. The limitations of using energy density in determining the process space has been discussed by Prashanth et al. for laser powder bed fusion [32]. On the other hand, Ng et al. factored in fluid flow in the melt pool, also known as Marangoni effect to better understand the escape of gas bubbles during the melting process [33]. Thus, the Marangoni equation can be used to estimate the velocity of the bubble in the liquid melt and is summarized in Equation 1 where v_{Mar} is the bubble velocity due to Marangoni flow, r is the bubble radius, η_{melt} is the viscosity of the melt, η_{gas} is the viscosity of the gas, σ is the surface tension, T is the temperature and y is the characteristic distance.

$$v_{Mar} = \frac{2}{3}\left(\frac{r}{2\eta_{melt} + 3\eta_{gas}}\right)\left(\frac{d\sigma}{dT}\right)\left(\frac{dT}{dy}\right) \ldots \text{(1)}$$

To compare the bubble velocity between the raster scan and coupon 10 for understanding the potential differences between the levels of gas porosity, the bubble velocity was calculated for different radii since a higher bubble velocity in the melt results in a higher probability of the bubble reaching the surface and escaping. The temperature gradient in the melt was calculated between the top and the bottom of the melt pool. The bubble velocity in the melt as a function of pore radius is shown in Figure 4(b) highlighting that the point melt coupon 10 has a higher bubble velocity compared to raster scan with the difference increasing as the gas bubbles increase in size thereby resulting in lower porosity. Although this model can describe the formation of pores it is a descriptive model rather than being predictive. Further, the temperature gradient used in the model is based on the simple conduction model compared to actual measured peak temperatures. The accuracy for estimation of relative gas porosity as a function of process parameters can be significantly improved by in-situ infrared thermography to estimate appropriate melt pool peak temperatures. More recently Vastola et al. developed a model for prediction of porosity during laser powder bed fusion, especially in high energy density regimes (>100 J/mm^3) [34]. However, their model can be used only for keyhole porosity and it is not clear whether the conditions in the current work result in keyholing. There is limited work in determining the possibility of keyhole porosity formation in electron beam powder bed fusion. Furthermore, their work makes assumptions regarding the characteristic fluid velocity in the melt pool that needs to be determined either experimentally or using intensive computational techniques. Therefore, this model was not deployed for the current study. Overall, we demonstrate that spot melting can be used to significantly reduce the porosity compared to raster melting using appropriate process parameters and discuss the variations in porosity based on a Marangoni flow model.

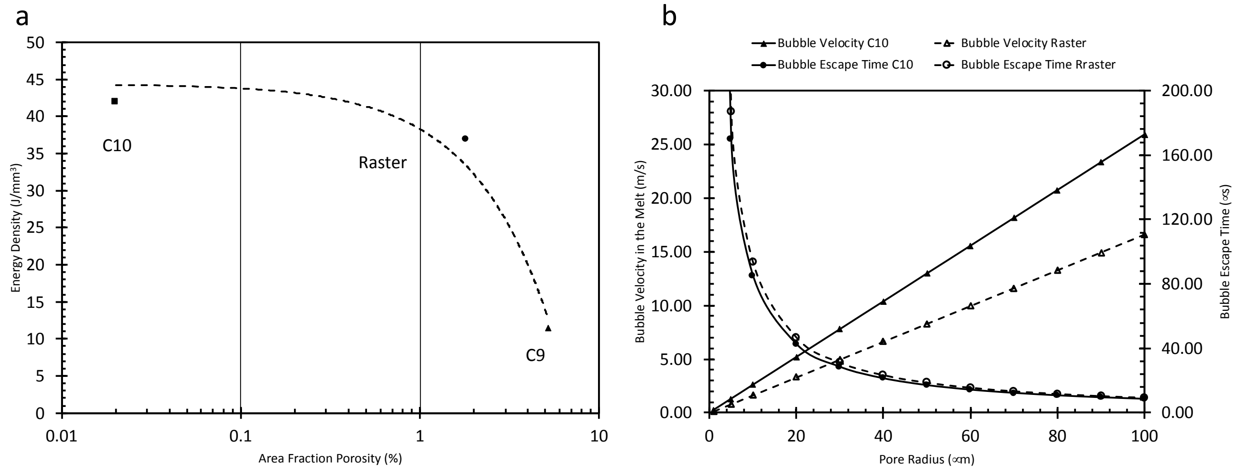

Figure 4 shows (a) the change in porosity area fraction as a function of energy density, and (b) compares the bubble escape velocity and escape time for point and raster melting

To better understand the microstructural evolution during spot melting, coupon 10 was subjected to OIM analysis. We analyzed the bulk microstructure as well as the microstructure at the top of the sample that experiences only a single melt-solidification event.

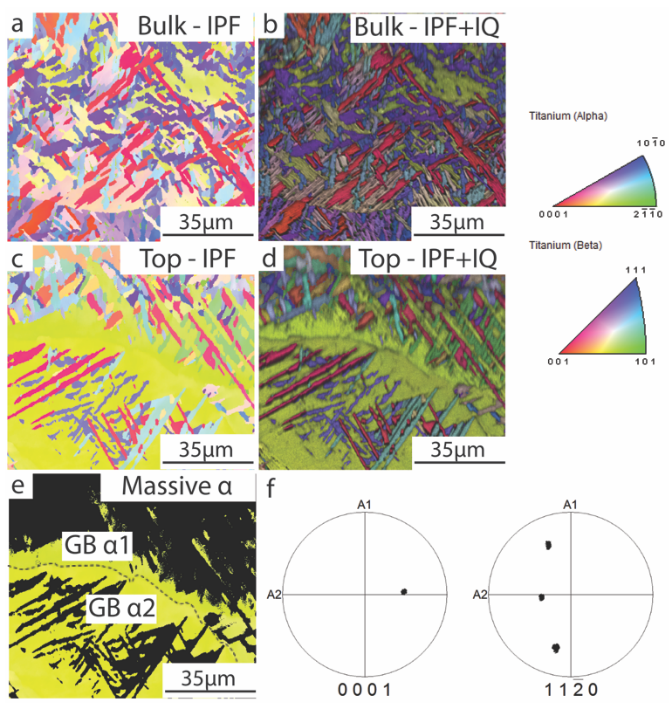

Figure 5 shows the IPF and IPF+IQ maps for regions in the bulk and the top of the sample along with the massive α and its corresponding pole figure showing the same orientation across the grain boundary for Coupon 10

Figure 5 (a and b) show the inverse pole figure (IPF) map and IPF map overlaid with image quality (IQ) map respectively for the bulk microstructure. The microstructure is primarily basketweave α along with small pockets of colony α growing from the prior β grain boundaries. The detailed crystallographic analysis of such microstructures has been presented by Bhattacharya et al [35,36]. Figure 5 (c and d) on the other hand show a fine martensitic microstructure at the topmost layer of the build that undergoes only one or two melting-solidification events. However, a closer look at the IPF map in Figure 5(c) in tandem with the IPF+IQ map in Figure 5(d) shows the presence of the same α variant on either side of the prior β-grain boundary. This is indicative of massive α growth during solidification and the one or two re-melt cycles are not enough for decomposition of this massive α. The α variants on either side of the grain boundary were isolated for further analysis (Figure 5e) and their corresponding pole figures show that they are indeed the same variant (Figure 5f). The formation of massive α co-existing with martensite during EBPF has been discussed by Lu et al. in their studies on raster melting of Ti-6Al-4V [37]. Although, they report much finer microstructure in the bulk compared to the microstructure obtained via spot melting in this paper, this difference is due to the deeper melt pool obtained during spot melting. The coarser microstructure combined with the extremely low levels of porosity obtained via spot melting can provide the best combination of fracture toughness and high cycle fatigue strength albeit at a minimal loss of the static strength. An in-depth mechanical characterization needs to be conducted to establish the material properties obtained via spot melting that is beyond the scope of this study.

Conclusions

In conclusion, we demonstrate for the first time that spot melting can be effectively used to significantly mitigate gas porosity compared to the traditional raster scan strategies used in EPBF of Ti-6Al-4V. The extremely low porosity levels are expected to result in a better HIP response and reduce the probability of pore reopening during subsequent heat treatments. Finally, we report that the deeper melt pools and lower cooling rates results in coarse basketweave a during spot melting. The process parameters can be further modified to result in pore free material with tailored microstructure. Single point melt pool simulations were conducted to quantify the observed microstructural features. A key limitation of single point simulations is their inability to determine thermal gradients during the course of an entire build. There is a need for development of analytical heat transfer models to better understand the evolution of thermal gradients and microstructures as a function of geometry during spot melting.

References

[1] L. Thijs, F. Verhaeghe, T. Craeghs, J. Van Humbeeck, J.P. Kruth, A study of the microstructural evolution during selective laser melting of Ti-6Al-4V, Acta Mater. 58 (2010) 3303–3312. doi:10.1016/j.actamat.2010.02.004.

[2] B. Vrancken, L. Thijs, J. Kruth, J. Van Humbeeck, Heat treatment of Ti6Al4V produced by selective laser melting_ microstructure and mechanical properties -Vranken

2012.pdf.crdownload, 541 (2012) 177–185.

[3] P. Nandwana, W.H. Peter, R.R. Dehoff, L.E. Lowe, M.M. Kirka, F. Medina, S.S. Babu, Recyclability Study on Inconel 718 and Ti-6Al-4V Powders for Use in Electron Beam Melting, Metall. Mater. Trans. B. 47 (2016) 754–762. doi:10.1007/s11663-015-0477-9.

[4] X. Shui, K. Yamanaka, M. Mori, Y. Nagata, K. Kurita, A. Chiba, Effects of post-processing on cyclic fatigue response of a titanium alloy additively manufactured by electron beam melting, Mater. Sci. Eng. A. 680 (2017) 239–248. doi:10.1016/j.msea.2016.10.059.

[5] C. de Formanoir, S. Michotte, O. Rigo, L. Germain, S. Godet, Electron beam melted Ti–6Al–4V: Microstructure, texture and mechanical behavior of the as-built and heat-treated material, Mater. Sci. Eng. A. 652 (2016) 105–119. doi:10.1016/j.msea.2015.11.052.

[6] H. Galarraga, D.A. Lados, R.R. Dehoff, M.M. Kirka, P. Nandwana, Effects of the microstructure and porosity on properties of Ti-6Al-4V ELI alloy fabricated by electron beam melting (EBM), Addit. Manuf. 10 (2016) 47–57. doi:10.1016/j.addma.2016.02.003.

[7] P. Nandwana, Y. Lee, C. Ranger, A.D. Rollett, R.R. Dehoff, S.S. Babu, Post-processing to Modify the α Phase Micro-Texture and β Phase Grain Morphology in Ti-6Al-4V Fabricated by Powder Bed Electron Beam Melting, Metall. Mater. Trans. A Phys. Metall. Mater. Sci. 50 (2019) 3429–3439. doi:10.1007/s11661-019-05247-4.

[8] X. Zhao, S. Li, M. Zhang, Y. Liu, T.B. Sercombe, S. Wang, Y. Hao, R. Yang, L.E. Murr, Comparison of the microstructures and mechanical properties of Ti-6Al-4V fabricated by selective laser melting and electron beam melting, Mater. Des. 95 (2016) 21–31. doi:10.1016/j.matdes.2015.12.135.

[9] J. Yang, H. Yu, Z. Wang, X. Zeng, Effect of crystallographic orientation on mechanical anisotropy of selective laser melted Ti-6Al-4V alloy, Mater. Charact. 127 (2017) 137–145. doi:10.1016/j.matchar.2017.01.014.

[10] J. Yang, H. Yu, J. Yin, M. Gao, Z. Wang, X. Zeng, Formation and control of martensite in Ti-6Al-4V alloy produced by selective laser melting, Mater. Des. 108 (2016) 308–318. doi:10.1016/j.matdes.2016.06.117.

[11] L.E. Murr, S.A. Quinones, S.M. Gaytan, M.I. Lopez, A. Rodela, E.Y. Martinez, D.H. Hernandez, E. Martinez, F. Medina, R.B. Wicker, Microstructure and mechanical behavior of Ti-6Al-4V produced by rapid-layer manufacturing, for biomedical applications, J. Mech. Behav. Biomed. Mater. 2 (2009) 20–32. doi:10.1016/j.jmbbm.2008.05.004.

[12] S.S. Al-Bermani, M.L. Blackmore, W. Zhang, I. Todd, The origin of microstructural diversity, texture, and mechanical properties in electron beam melted Ti-6Al-4V, Metall. Mater. Trans. A Phys. Metall. Mater. Sci. 41 (2010) 3422–3434. doi:10.1007/s11661-010-0397-x.

[13] K. Puebla, L. E. Murr, S. M. Gaytan, E. Martinez, F. Medina, R. B. Wicker, Effect of Melt Scan Rate on Microstructure and Macrostructure for Electron Beam Melting of Ti-6Al-4V, Mater. Sci. Appl. 03 (2012) 259–264. doi:10.4236/msa.2012.35038.

[14] M. Seifi, M. Dahar, R. Aman, O. Harrysson, J. Beuth, J.J. Lewandowski, Evaluation of Orientation Dependence of Fracture Toughness and Fatigue Crack Propagation Behavior of As-Deposited ARCAM EBM Ti-6Al-4V, Jom. 67 (2015) 597–607. doi:10.1007/s11837-015-1298-7.

[15] J.J. Lewandowski, M. Seifi, Metal Additive Manufacturing: A Review of Mechanical

Properties, Annu. Rev. Mater. Res. 46 (2016) 151–186. doi:10.1146/annurev-matsci-070115-032024.

[16] M. Seifi, A. Salem, D. Satko, J. Shaffer, J.J. Lewandowski, Defect distribution and microstructure heterogeneity effects on fracture resistance and fatigue behavior of EBM Ti–6Al–4V, Int. J. Fatigue. 94 (2017) 263–287. doi:10.1016/j.ijfatigue.2016.06.001.

[17] R. Cunningham, A. Nicolas, J. Madsen, E. Fodran, E. Anagnostou, M.D. Sangid, A.D. Rollett, Analyzing the effects of powder and post-processing on porosity and properties of electron beam melted Ti-6Al-4V, Mater. Res. Lett. 5 (2017) 516–525. doi:10.1080/21663831.2017.1340911.

[18] R. Cunningham, S.P. Narra, T. Ozturk, J. Beuth, A.D. Rollett, Evaluating the Effect of Processing Parameters on Porosity in Electron Beam Melted Ti-6Al-4V via Synchrotron X-ray Microtomography, JOM. 68 (2016) 765–771. doi:10.1007/s11837-015-1802-0.

[19] S. Tammas-Williams, P.J. Withers, I. Todd, P.B. Prangnell, The Influence of Porosity on Fatigue Crack Initiation in Additively Manufactured Titanium Components, Sci. Rep. 7 (2017) 7308. doi:10.1038/s41598-017-06504-5.

[20] P. Nandwana, M.M. Kirka, V.C. Paquit, S. Yoder, R.R. Dehoff, Correlations Between Powder Feedstock Quality, In Situ Porosity Detection, and Fatigue Behavior of Ti-6Al-4V Fabricated by Powder Bed Electron Beam Melting: A Step Towards Qualification, JOM. 70 (2018) 1686–1691. doi:10.1007/s11837-018-3034-6.

[21] S. Tammas-Williams, P.J. Withers, I. Todd, P.B. Prangnell, The Effectiveness of Hot Isostatic Pressing for Closing Porosity in Titanium Parts Manufactured by Selective Electron Beam Melting, Metall. Mater. Trans. A Phys. Metall. Mater. Sci. 47 (2016) 1939–

1946. doi:10.1007/s11661-016-3429-3.

[22] S. Tammas-Williams, P.J. Withers, I. Todd, P.B. Prangnell, Porosity regrowth during heat treatment of hot isostatically pressed additively manufactured titanium components, Scr. Mater. 122 (2016) 72–76. doi:10.1016/j.scriptamat.2016.05.002.

[23] S. Tammas-Williams, H. Zhao, F. Léonard, F. Derguti, I. Todd, P.B. Prangnell, XCT analysis of the influence of melt strategies on defect population in Ti-6Al-4V components manufactured by Selective Electron Beam Melting, Mater. Charact. 102 (2015) 47–61. doi:10.1016/j.matchar.2015.02.008.

[24] R.R. Dehoff, M. Kirka, W.J. Sames, H. Bilheux, A.S. Tremsin, L.E. Lowe, S.S. Babu, Site specific control of crystallographic grain orientation through electron beam additive manufacturing, Mater. Sci. Technol. (United Kingdom). 31 (2015) 931–938. doi:10.1179/1743284714Y.0000000734.

[25] M.M. Kirka, Y. Lee, D.A. Greeley, A. Okello, M.J. Goin, M.T. Pearce, R.R. Dehoff, Strategy for Texture Management in Metals Additive Manufacturing, Jom. 69 (2017) 523–531. doi:10.1007/s11837-017-2264-3.

[26] Y.S. Lee, M.M. Kirka, R.B. Dinwiddie, N. Raghavan, J. Turner, R.R. Dehoff, S.S. Babu, Role of scan strategies on thermal gradient and solidification rate in electron beam powder bed fusion, Addit. Manuf. 22 (2018) 516–527. doi:10.1016/j.addma.2018.04.038.

[27] N. Raghavan, R. Dehoff, S. Pannala, S. Simunovic, M. Kirka, J. Turner, N. Carlson, S.S. Babu, Numerical modeling of heat-transfer and the influence of process parameters on tailoring the grain morphology of IN718 in electron beam additive manufacturing, Acta Mater. 112 (2016) 303–314. doi:10.1016/j.actamat.2016.03.063.

[28] R. Rai, J.W. Elmer, T.A. Palmer, T. Debroy, Heat transfer and fluid flow during keyhole mode laser welding of tantalum, Ti-6Al-4V, 304L stainless steel and vanadium, J. Phys. D. Appl. Phys. 40 (2007) 5753–5766. doi:10.1088/0022-3727/40/18/037.

[29] H. Wang, Y. Zou, Microscale interaction between laser and metal powder in powder-bed additive manufacturing: Conduction mode versus keyhole mode, Int. J. Heat Mass Transf. 142 (2019) 118473. doi:10.1016/j.ijheatmasstransfer.2019.118473.

[30] V. Juechter, T. Scharowsky, R.F. Singer, C. Körner, Processing window and evaporation phenomena for Ti-6Al-4V produced by selective electron beam melting, Acta Mater. 76 (2014) 252–258. doi:10.1016/j.actamat.2014.05.037.

[31] R. Cunningham, S.P. Narra, C. Montgomery, J. Beuth, A.D. Rollett, Synchrotron-Based X-ray Microtomography Characterization of the Effect of Processing Variables on Porosity Formation in Laser Power-Bed Additive Manufacturing of Ti-6Al-4V, Jom. 69 (2017) 479–484. doi:10.1007/s11837-016-2234-1.

[32] K.G. Prashanth, S. Scudino, T. Maity, J. Das, J. Eckert, Is the energy density a reliable parameter for materials synthesis by selective laser melting?, Mater. Res. Lett. 5 (2017) 386–390. doi:10.1080/21663831.2017.1299808.

[33] G.K.L. Ng, A.E.W. Jarfors, G. Bi, H.Y. Zheng, Porosity formation and gas bubble retention in laser metal deposition, Appl. Phys. A Mater. Sci. Process. 97 (2009) 641–649. doi:10.1007/s00339-009-5266-3.

[34] G. Vastola, Q.X. Pei, Y.W. Zhang, Predictive model for porosity in powder-bed fusion additive manufacturing at high beam energy regime, Addit. Manuf. 22 (2018) 817–822. doi:10.1016/j.addma.2018.05.042.

[35] D. Bhattacharyya, G.. Viswanathan, R. Denkenberger, D. Furrer, H.L. Fraser, The role of crystallographic and geometrical relationships between α and β phases in an α/β titanium alloy, Acta Mater. 51 (2003) 4679–4691. doi:10.1016/S1359-6454(03)00179-4.

[36] D. Bhattacharyya, G.B. Viswanathan, H.L. Fraser, Crystallographic and morphological relationships between β phase and the Widmanstätten and allotriomorphic α phase at special β grain boundaries in an α/β titanium alloy, Acta Mater. 55 (2007) 6765–6778. doi:10.1016/j.actamat.2007.08.029.

[37] S.L. Lu, M. Qian, H.P. Tang, M. Yan, J. Wang, D.H. StJohn, Massive transformation in Ti–6Al–4V additively manufactured by selective electron beam melting, Acta Mater. 104 (2016) 303–311. doi:10.1016/j.actamat.2015.11.011.

Acknowledgements

Research was performed at the U.S. Department of Energy's Manufacturing Demonstration Facility, located at Oak Ridge National Laboratory. Research was sponsored by the U.S. Department of Energy, Office of Energy Efficiency and Renewable Energy, Advanced Manufacturing Office, under Contract DE-AC05-00OR22725 with UT-Battelle, LLC.